AIAA-2004-0004

MEAN FLOW AND ACOUSTICS OF DUAL-STREAM JETS

Dimitri Papamoschou *
University of California, Irvine, California 92697-3975

This study examines the connection between the mean flow shape and the acoustic emission of dual-stream jets. The experimental investigation encompassed jets issuing from coaxial, eccentric, and arcuate nozzles, as well as nozzles with deflectors in the secondary stream. The inflection points of the transverse velocity profile were used to define the generalized secondary core (GSC) of the jet. In coaxial and arcuate jets, the length of the GSC roughly equals that of the secondary potential core. In eccentric jets and in jets with deflection of the bypass stream, the GSC is much longer than the secondary potential core. As a result, a long secondary shear layer is formed that reduces the primary convective Mach number throughout the dominant noise source region. The acoustic results indicate that, when the GSC is shorter than the primary potential core, noise reduction is modest, whereas when the GSC is longer than the primary potential core, noise reduction is substantial. The mean flow data were distilled into simple models for the primary and secondary convective Mach number distributions. The jet with deflected secondary flow achieved the lowest average convective Mach number and produced the largest noise reduction.

Nomenclature

a	=	mean speed of sound
B	=	bypass ratio, $\dot{m}_s/\dot{m}_p$
D	=	nozzle diameter
D_m	=	mass-flux-equivalent diameter, Eq. 12
$\dot{m}$	=	mass flow rate
L	=	length of potential core
M	=	Mach number
M_c	=	convective Mach number
u	=	mean velocity in jet plume
U	=	nozzle-exit velocity
U_c	=	convective velocity
x	=	axial coordinate from nozzle exit
δ'	=	shear layer growth rate
ρ	=	density

Subscripts

p	=	primary (core) exhaust
s	=	secondary (bypass) exhaust
∞	=	flight conditions

*Professor, Associate Fellow AIAA

Copyright ©2004 by D. Papamoschou. Published by the American Institute of Aeronautics and Astronautics, Inc. with permission.

Introduction

The dominant component of jet noise is due to the mixing of large-scale turbulent eddies. Large-scale mixing noise has been successfully modeled by treating the eddies as instability waves [1, 2, 3, 4]. A governing parameter is the convective Mach number M_c of the instability wave. When M_c is supersonic, strong Mach wave radiation is evident in instantaneous photographic realizations of jets. For subsonic M_c, the growth-decay nature of instability waves creates a spectrum of phase speeds, part of which is supersonic [2]. The resulting Mach wave emission is not as intense or nonlinear as its supersonic counterpart but still constitutes the strongest source of sound. As M_c becomes more subsonic, Mach wave emission (that is, the acoustic energy propagated to the far field by supersonic disturbances) weakens rapidly. This has spurred recent attempts to reduce M_c by strategic use of a secondary flow. These works suggest that noise reduction is intimately connected to the shape of the mean flow [5, 10].

This paper attempts to shed more light on the relation between noise emission of dual-stream jets and their mean flow characteristics. We look at several nozzle shapes, some of which provide noise reduction and some that do not, and try to explain the

conditions under which noise reduction is achievable. The first step is identification of the key elements of the mean flow that distinguish a dual-stream jet from a single-stream jet. It is followed by development of simple models for the velocity distributions that define the primary and secondary shear layers. This leads to a model for the convective Mach numbers that can be used as a guide for assessing which configurations have the potential for significant noise reduction.

Elements of the Mean Flow

The initial region of a dual-stream jet consists of two shear layers: primary and secondary. See Fig. 1. The primary shear layer encloses the primary potential core. The region between the primary and secondary shear layers defines the generalized secondary core which contains an initial potential region followed by a non-potential region. The concept of a generalized secondary core (GSC) is essential for understanding the acoustic benefit of certain dual-stream configurations. In many practical cases, for instance in coaxial jets of turbofan engines, the GSC ends upstream of the end of the primary core. The flow past the end of the GSC consists of single shear layer between the jet centerline and the ambient stream, thus has the characteristics of a single-stream jet. It is useful therefore to divide the jet flow into two regions: the *compound* region, which is the region before the end of the GSC; and the *simple* region, which is the region past the end of the GSC. The extent of the compound region, relative to the length of the primary potential core, is critical for noise reduction.

The relations for the primary and secondary convective Mach numbers are as follows:

$$M_{c_p}(x) = \frac{U_{c_p}(x) - u_s(x)}{a_s(x)} \quad (1)$$

$$M_{c_s}(x) = \frac{U_{c_s}(x) - U_\infty}{a_\infty} \quad (2)$$

Application of Eqs. 1 and 2 requires knowledge of the velocity distributions $u_p(x)$ and $u_s(x)$ that define the two shear layers. Once these distributions are known, the convective velocities $U_{c_p}(x)$ and $U_{c_s}(x)$ can be estimated from empirical models derived from direct measurements of U_c in jets and shear layers [8] (see Eqs. 18-20).

The fast velocity of the primary shear layer, $u_p(x)$, is the maximum mean velocity of the jet. Experiments show that it occurs on the axis of the primary jet, even for configurations with asymmetric secondary flow. Definition of the slow velocity of the primary shear layer (fast velocity of the secondary shear layer), $u_s(x)$, is not as straight-forward. It is clear that $u_s(x) = U_s$ inside the potential region of the GSC. Downstream of the potential region, however, definition of $u_s(x)$ becomes problematic. Experimental velocity profiles show a distinct secondary layer for a finite distance past the end of the secondary potential core. This is particularly noticeable in jets from eccentric nozzle configurations (see for example Fig. 4c of [6].) It would be unreasonable, therefore, to assume that the effect of the secondary flow ceases immediately past the end of the secondary potential core.

The resolution to this dilemma entails a consistent, unambiguous way to detect the presence of a secondary shear layer. This is done here by examining the inflection points of the radial velocity profile. The compound region of the jet is characterized by three inflection points: $i1$, $i2$, and $i3$, marked in Fig. 1. The second inflection point, $i2$, defines the lower edge of the primary shear layer (upper edge of the secondary shear layer). Dahl and Morris [7], in their mean-flow model for coaxial jets, used basically the same criterion to distinguish the two shear layers. Thus $u_s(x) = u[x, y_{i2}(x)]$. The three inflection points persist for a certain distance past the end of the secondary potential core. At some point, two of them disappear and the profile reduces to that of a single-stream jet. The downstream distance where the number of inflection points reduces from three to one marks the end of the GSC. Beyond this point, $u_s = U_\infty$ and $a_s = a_\infty$ in Eq. 1. Also, M_{c_s} (Eq. 2) ceases to exist.

To reduce M_{c_p} throughout the jet it is necessary to have a long GSC that covers the entire primary potential core. Eccentric nozzle arrangements have proven to be very effective in this respect. The experiments of Murakami and Papamoschou [6] showed that eccentric nozzles shorten the length of the primary potential core and double the length of the secondary potential core on the underside of the jet. The downward noise emission of the eccentric jet was much lower than the noise emission of the equivalent coaxial jet [5]. A critical flow feature that was not emphasized in Ref. [6] is the remarkable persistence of the inflection point $i2$ in the eccentric cases with velocity ratio $U_s/U_p = 0.67$. Reexamination of the relevant data of Ref. [6] shows

that the inflection point $i2$ (and, of course, the inflection points $i1$ and $i3$) can be identified all the way to the end of the measurement region. In other words, by offsetting the nozzles, the GSC on the underside of the jet became longer than the primary potential core. This may explain the acoustic benefit of eccentric configurations even with small diameter ratio and small secondary mass flow rate [5].

Mean Velocity Data

We now apply the above procedures to mean flow data collected over a number of years in the UCI Supersonic Turbulence Laboratory. The investigations have encompassed a variety of jets issuing from coaxial, eccentric, and arcuate nozzles, as well as from nozzles with deflectors in the secondary (bypass) stream [6, 10]. For brevity, we will refer to the jet issued from the latter nozzle as the "deflected" jet. Figure 2 shows the generic nozzle geometries. The eccentric arrangement was obtained by totally offsetting the primary nozzle so that the outer surface of the primary nozzle touched the inner wall of the secondary nozzle. The arcuate nozzle featured a smooth transition from a full annulus at the nozzle entrance to a 240° annulus at the nozzle exit. The coaxial nozzle with deflectors in the bypass stream featured two square vanes mounted inside the bypass duct, as shown in Fig. 2(d). The vane width equaled the thickness of the annular bypass duct and the vane trailing edges coincided with the duct exit. The vane angle of attack was 20°. The vanes imparted a downward tilt to the secondary plume, in effect creating eccentricity not at the nozzle exit but further downstream in the jet plume.

Compressed air, supplied at room temperature, was fed to both the primary and secondary nozzles. Nozzle configurations and flow conditions are summarized in Tables 1 and 2. For ease of reference we use a labeling system that describes the size and shape of the secondary nozzle and the velocity ratio. Coaxial nozzles are denoted by Cxx, arcuate nozzles by Axx, eccentric nozzles by Exx, and coaxial nozzles with vanes in the secondary stream by Vxx, where $xx = 10 \times D_s/D_p$. The velocity ratio is denoted by Ryy, where $yy = 100 \times U_s/U_p$. Case C20R67, for example, describes the coaxial jet with $U_s/U_p = 0.67$ issuing from a coaxial nozzle with $D_s/D_p = 2.0$. Not all combinations of nozzles and velocity ratios were covered. Table 3 lists the combinations for which full surveys of the velocity field were obtained. Detailed flow field comparisons will be made between the cases of the second group of Table 3, i.e, cases A18R71, C16R71, E16R71, and V16R71. They all share the same flow conditions and same exit areas.

We now present selected results that capture the behavior of the flow from the various nozzle geometries. Figure 3 plots iso-contours of u/U_p for jets issuing from the following nozzles: clean coaxial, arcuate, eccentric, and coaxial with vanes in the secondary stream. Focusing in the region near the end of the potential core, defined here by the contour $u/U_p = 0.9$, we make the following observations. For the clean coaxial jet, there is no indication of a secondary layer. The secondary stream is fully mixed with the primary flow well upstream of the end of the primary potential core. The same holds true in the arcuate case, even though the secondary potential core is moderately longer than that of the coaxial case. In the eccentric and deflection cases, however, there is a distinct layer of low-speed flow on the underside of the jet. It is notable that, even though the coaxial jet with vanes mixes slower than the eccentric jet, the relative coverage of the primary flow by the secondary flow appears roughly the same in both cases.

We now slice the velocity field on the $y - z$ plane passing through the end of the primary potential core ($x = L_p$) for each of the flows of Fig. 3. Figure 4 shows iso-contour plots of $u(L_p, y, z)/u(L_p, 0, 0)$. The arcuate jet shows only minor asymmetry compared to the coaxial case and there is no discernible secondary layer. The eccentric and vane arrangements show a substantial concentration of secondary layer on the underside of the jet.

To determine the inflection points, the second $y-$ derivative of the velocity profiles was computed using a Savitzky-Golay smoothing filter [9]. Figure 5 plots the loci of the inflection points $i1$, $i2$, and $i3$ corresponding to the mean flow surveys of Fig. 3. Using the concept of the generalized secondary core (GSC) as per Fig. 1, we observe that the GSC is very short for the coaxial and arcuate cases, and very long for the eccentric and deflected cases. In fact, for the latter two cases the inflection point $i2$ persists all the way to the end of the measurement region. This is a dramatic change that cannot be explained solely by the thickening of the secondary flow near the nozzle exit. Fig. 6 plots the distributions $u_p(x)$ and $u_s(x)$ that define the jet shear layers. As mentioned earlier, $u_p(x)$ is the velocity along

the jet centerline and $u_s(x)$ is the velocity along the inflection point $i2$. In the coaxial case, $u_s(x)$ decays very rapidly past the end of the GSC. In the eccentric and deflected jets the decay of $u_s(x)$ is much more gradual and reflects the long GSCs created in those jets. The decay rate in the deflected jet is moderately faster than that in the eccentric case.

Using the convective Mach number model of Murakami and Papamoschou [8], the distributions $M_{c_p}(x)$ and $M_{c_s}(x)$ are computed and plotted in Fig. 7. It should be understood that, because the experiments used air at room temperature, the convective Mach numbers calculated here are lower than those in hot jets. However, the trends seen below are expected to hold for hot jets with similar velocity ratio as the cold jets. For the coaxial jet, M_{c_p} is very low subsonic at the jet exit but rises rapidly past the end of the GSC and reaches the peak value of 0.58 at the axial location where the GSC ends (x/D_p=4). Offsetting the nozzles to an eccentric arrangement reduces the maximum value of M_{c_p} on the underside of the jet to 0.15. The very slow decay of $u_s(x)$ creates a long distribution of M_{c_s}, starting from 0.32 at the nozzle exit and ending at 0.25 near the end of the measurement region. This suggests that the secondary layer now becomes the dominant noise source. In the deflected jet, the maximum value of M_{c_p} is 0.25, higher than in the eccentric case, but the distribution of M_{c_s} is shorter and its average value is lower. The deflected jet seems to achieve a better balance between the distributions of M_{c_p} and M_{c_s} than does the eccentric jet. Of course this depends on the tilt angle and other details of the deflection mechanism. Nevertheless, the deflection approach allows more degrees of freedom to manipulate the distributions of M_{c_p} and M_{c_s} (not only in the downward direction but also in the sideline direction) for optimal noise reduction.

Acoustic Data

In this section we compare far-field acoustic spectra in the direction of peak sound emission for selected dual-stream jets issuing from the four nozzle shapes considered in this study (coaxial, arcuate, eccentric, and coaxial with vanes in the bypass stream). For asymmetric cases, the spectra were measured on the lower (quiet) hemisphere. Helium-air mixtures were used to match the velocity and density of a heated jet. Experiments were conducted in UCI's Jet Aeroacoustics Facility, described in earlier publications [5].

The first comparison is between the coaxial and arcuate jets. The flow conditions were $U_p = 600$ m/s, $U_s = 400$ m/s, and $B = 2.2$. Figure 8(a) shows that the arcuate jet is only slightly quieter the coaxial jet. Recall that the GSC of the arcuate jet was moderately longer than that of the coaxial jet but did not reach the end of the primary potential core. (Fig. 5). Consequently, the region of strong noise sources was not adequately covered by the secondary flow, which explains why the arcuate jet was nearly as loud as the coaxial jet.

We now turn to the eccentric and deflected cases. In the comparisons that follow, the flow conditions were $U_p = 580$ m/s, U_s=360 m/s, and $B = 1.8$. As seen in Figs. 8b and 8c, the eccentric and deflected jets produce substantial noise reduction relative to the coaxial jet, with the deflected jet having a distinct advantage. This is consistent with the long secondary cores created in these cases, as observed in Fig. 5. The advantage of the deflected jet may be attributed to the better balance of M_{c_p} and M_{c_s} than in the eccentric jet. The spectra of Fig. 8 exemplify the trends measured in many additional jets. When the GSC reaches past the end of the primary potential core, a substantial drop in large-scale noise is observed. Otherwise, noise reduction is modest or nil.

Mean Flow Model

In this section we attempt to distill the mean velocity data into simple, universal models for the velocity distributions $u_p(x)$ and $u_s(x)$ in coaxial, eccentric, and deflected jets. We do not consider arcuate jets because they obviously have little acoustic value. This exercise is no substitute for a full computation or experimental survey. Instead, its intent is to provide scaling laws that can be used as guidance in predicting the acoustic benefit of a jet. Central to this effort is the use of the "classical" formula for the growth rate of a fully-turbulent, planar shear layer [11]. As we discuss the mean-flow trends, we will be developing equations that will be listed in the latter part of this section. Even though all the testing was done at static conditions, the expressions will be generalized to flight conditions by assuming that the trends observed at static conditions hold in a frame of reference moving with velocity U_∞.

Basic Trends

The first step is to seek the proper scaling for correlating the axial velocity distributions. Figure 9 plots the distribution of $u_p(x)$ in an absolute frame of reference for all the cases of Table 3 except for the arcuate jet. The large variations in these distributions reflect the variations in primary potential core length, L_p, as well as the variations in mass flow rate of the various jets. Earlier study of dual-stream jets showed that the effect of variable mass flow rate can be filtered out by normalizing the axial coordinate by the mass-flux-equivalent diameter, D_m. The proper correlation parameter, therefore, should be $(x - L_p)/D_m$, with L_p obtained from the theoretical model of Eqs. 8-10. Figure 7 shows that it does a fair job of collapsing the data. Importantly, the slopes in the decaying region are all very close to 0.1, that is:

$$\frac{d(U_p/u_p)}{d(x/D_m)} \approx 0.1$$

This allows us to construct the piecewise-linear model of Eq. 11, which is overlaid on Fig. 10.

Construction of a model for $u_s(x)$ (the velocity along the inflection point $i2$) is more challenging. As shown in Fig. 11, when we plot $us(x)$ in an absolute frame of reference the trends are even more varied than for the centerline velocity. It is apparent that there is a substantial difference between the coaxial distributions and the distributions for the eccentric and deflected jets. So it makes sense to look at each type separately. Experimentation with various scaling parameters showed that the best correlations are obtained when the axial coordinate is normalized by the area-equivalent diameter of the secondary flow, $D_{s,\mathrm{eq}}$. Also, we shift the frame of reference from x to $x - L_s$, where L_s is the theoretical length of the secondary potential core (Eq. 6). Figure 12 plots the distributions of $u_s(x)$ for the coaxial cases using the proper correlation parameter $(x - L_s)/D_{s,\mathrm{eq}}$. There is reasonable collapse of the plots, and all the plots terminate one or two equivalent diameters past the end of the secondary potential core. An elliptical distribution, given by Eq. 14, simulates the rapid decay of $u_s(x)$ for $x > L_s$.

Figure 13 applies the same type of correlation to the eccentric data. Here we observe a large difference between cases that have velocity ratio U_s/U_p around 0.7 and those with smaller velocity ratio. The former ones exhibit a slow decay that can be approximated by the piecewise-linear model of Eq. 15.

The cases with low velocity ratio behave similarly to the coaxial jets. Given that in civil turbofan engines the velocity ratio is around 0.7, the cases highlighted in Fig. 12 have the most practical relevance and are emphasized here. One of the $U_s/U_p = 0.67$ cases in Fig. 12 departs from the model at large values of $(x - L_s)/D_{s,\mathrm{eq}}$. This particular flow, E14R67, has a thin coflow annulus and very small value of the bypass ratio (0.52), thus is not representative of commercial turbofan engines. Finally, Fig. 14 plots the distribution of $u_s(x)$ for the deflected jet. As with the eccentric cases, a piecewise-linear model, but with larger slope (faster decay), works reasonably well (Eq. 16).

Analytical Model

We now construct mathematical relations for the trends observed in Figures 10, 12, 13 and 14, and combine them with expressions for the lengths of the primary and secondary potential cores. The analysis presented here is based in large part on the work of [6]. The reader should refer to it for more background. We start with the "classical" formula for the growth rate of a fully-turbulent, planar shear layer,

$$\delta'(\mathcal{R},\mathcal{S},M_{c,\mathrm{sym}}) = 0.14\frac{(1-\mathcal{R})(1+\sqrt{\mathcal{S}})}{1+\mathcal{R}\sqrt{\mathcal{S}}}\times \left[0.23 + 0.77\exp(-3.5M_{c,\mathrm{sym}}^2)\right] \quad (3)$$

where $\mathcal{R}$ is the velocity ratio, $\mathcal{S}$ is the density ratio, and $M_{c,\mathrm{sym}}$ is the symmetric convective Mach number. In developing relations for the primary potential core length, two reference flows are important: the single jet and the coflowing jet (i.e., a jet immersed in an infinite coflowing stream). The potential core length of the single jet is

$$\frac{L_{\mathrm{single}}}{D_p} = \left\{\delta'\left(0, \frac{\rho_\infty}{\rho_p}, \frac{U_p}{a_p + a_\infty}\right)\right\}^{-1} \quad (4)$$

and the potential core length of the coflowing jet is

$$\frac{L_{\mathrm{coflowing}}}{D_p} = \left\{\delta'\left(\frac{U_s}{U_p}, \frac{\rho_s}{\rho_p}, \frac{U_p + U_s}{a_p + a_s}\right)\right\}^{-1} \quad (5)$$

The length of the secondary potential core is

$$\frac{L_s}{D_p} = 2.8\frac{H}{D_p}\left[\frac{L_{\mathrm{coflowing}}/D_p}{\delta_s' L_{\mathrm{coflowing}}/D_p + 1}\right] \quad (6)$$

where

$$\delta_s' = \delta'\left(\frac{U_\infty}{U_p}, \frac{\rho_\infty}{\rho_s}, \frac{U_s - U_\infty}{a_s + a_\infty}\right) \quad (7)$$

and H is the exit thickness of the secondary stream. Eqs. 6 and 7 apply to all the types of jets. Note that, for the eccentric case, H is double that of the corresponding coaxial case.

Primary potential core lengths

For coaxial jets, the basic idea is that the length of the primary potential core core, L_p, lies somewhere between the potential core length of the single jet, L_{single}, and the potential core length of the coflowing jet, $L_{\text{coflowing}}$, by an amount dependent on the length of the secondary potential core, L_s.

$$\frac{L_p}{L_{\text{single}}} = 1 + \tanh\left(2.8\frac{L_s}{L_{\text{coflowing}}}\right) \times \left(\frac{L_{\text{coflowing}} - L_{\text{single}}}{L_{\text{single}}}\right) \tag{8}$$

For the eccentric jet, experiments show that the length of the primary core is roughly equal to that of the single jet:

$$L_p = L_{\text{single}} \tag{9}$$

In the case of the deflected jet, the limited experiments so far indicate that the primary potential core is about 15% shorter than that of the coaxial case,

$$\frac{L_p}{L_{\text{single}}} = 0.85\left[1 + \tanh\left(2.8\frac{L_s}{L_{\text{coflowing}}}\right) \times \left(\frac{L_{\text{coflowing}} - L_{\text{single}}}{L_{\text{single}}}\right)\right] \tag{10}$$

Centerline velocity distribution

The centerline velocity distribution for all the jets is captured by the model of Fig. 9:

$$(u_p(x) - U_\infty)/(U_p - U_\infty) = \begin{cases} 1, & x \le L_p \\ (1 + 0.1(x - L_p)/D_m)^{-1}, & x > L_p \end{cases} \tag{11}$$

where

$$D_m = D_p\sqrt{1 + B} \tag{12}$$

is the mass-flux-equivalent diameter.

Velocity distribution along i2

The velocity distribution along the inflection point $i2$ exhibits different behavior for the various jet types. For all jets, however, scaling based on the area-equivalent diameter of the secondary stream

$$D_{s,\text{eq}} = \sqrt{\frac{4A_s}{\pi}} \tag{13}$$

produces the best collapse of the data. For coaxial jets,

$$(u_s(x) - U_\infty)/(U_s - U_\infty) = \begin{cases} 1, & x \le L_s \\ \sqrt{1 - \left(\frac{x - L_s}{2D_{s,\text{eq}}}\right)^2}, & L_s \le x < L_s + 2D_{s,\text{eq}} \\ 0 & x > L_s + 2D_{s,\text{eq}} \end{cases} \tag{14}$$

For eccentric jets with velocity ratio $U_s/U_p \sim 0.7$,

$$(u_s(x) - U_\infty)/(U_s - U_\infty) = \begin{cases} 1, & x \le L_s \\ (1 + 0.05(x - L_s)/D_{s,\text{eq}})^{-1}, & x > L_s \end{cases} \tag{15}$$

For jets with deflection of the bypass stream,

$$(u_s(x) - U_\infty)/(U_s - U_\infty) = \begin{cases} 1, & x \le L_s \\ (1 + 0.1(x - L_s)/D_{s,\text{eq}})^{-1}, & x > L_s \end{cases} \tag{16}$$

Equations 8-16 allow evaluation of the axial distributions of the velocities defining the primary and secondary shear layers for the various jet types. The corresponding values of speed of sound and Mach number are obtained by assuming that the mean total temperature, T_0, obeys the Crocco-Busemann relation

$$T_0(x) = \frac{T_{0e}u_i - T_{0i}u_e}{u_i - u_e} + \frac{T_{0i} - T_{0e}}{u_i - u_e}u(x) \tag{17}$$

where subscripts i and e represent the initial and final conditions, respectively, of each axial distribution.

Convective Mach number

Prediction of the convective Mach number is based on the empirical formulae proposed by Murakami & Papamoschou [8]. Considering a shear layer between a fast stream (1) and a slow stream (2), the convective Mach number of eddies relative to the slow stream is

$$M_c = M_{c,\text{sym}} + \frac{d}{\sqrt{1 + (a_2/a_1)^2}} \tag{18}$$

where

$$M_{c,\text{sym}} = \frac{u_1 - u_2}{a_1 + a_2}, \tag{19}$$

and

$$d = \begin{cases} 1.25\ln M_{c,\text{sym}} + 1.11 & , M_{c,\text{sym}} > 0.41 \\ 0 & , M_{c,\text{sym}} \le 0.41 \end{cases} \tag{20}$$

Application to Turbofan Exhaust

It is instructive to apply the above model to a flow of practical significance. We consider a turbofan engine with bypass ratio $B = 5$ at the following exhaust conditions: $M_p = 0.90$, $U_p = 460$ m/s, $M_s = 0.95$, and $U_s = 335$ m/s. Figure 15 plots the convective Mach number distributions on the underside of coaxial, eccentric, and deflected exhausts at static condition. In the coaxial case, the secondary potential core is 50% shorter than the primary potential core. Because the velocity u_s decays very fast past the end of the secondary potential core, a large portion of the primary potential core is "exposed" to the ambient. Consequently, the primary convective Mach number M_{c_p} reaches high values, around 0.85, near the end of the primary potential core.

With an eccentric nozzle, the generalized secondary core (GSC) is very long and, as a result, M_{c_p} is very low throughout the jet. The distribution of M_{c_s} is correspondingly long and at relatively high levels, ranging from 0.6 at the jet exit to 0.4 at $x/D_p = 30$. This suggests that the secondary flow becomes the dominant noise generator. In the case of the deflected jet, near the end of the primary potential core M_{c_s} and M_{c_p} reach about the same value. From an average standpoint, over the first 30 diameters, the deflected jet achieves the lowest values of convective Mach numbers. Figure 16 makes the same comparisons at forward flight. There is an overall reduction in the levels of convective Mach numbers. Also, both the primary and secondary potential cores elongate relative to the static case, with the secondary potential core elongating the furthest. The trends are the same as in the static case. Again, the deflected jet achieves the lowest average convective Mach number.

Concluding Remarks

This work introduces the concept of a generalized secondary core (GSC) for a dual-stream jet, defined by the inflection points of the velocity profile as per Fig. 1. In a coaxial or arcuate jet, the length of the GSC roughly equals that of the secondary potential core. In eccentric and deflected jets (coaxial jets where the secondary plume is tilted relative to the primary plume), the GSC is much longer than the secondary potential core. As a result, a long secondary shear layer is formed that reduces the primary convective Mach number throughout the dominant noise source region. It is important to realize that the GSC does not contain only secondary fluid. In fact, it may be irrelevant what the composition of the flow is. The important thing is to generate the three inflection points as illustrated in Fig. 1.

Several past studies have identified the end of the primary potential core, $x = L_p$, as the region of strong noise generation [13, 12]. The experiments of this study indicate that when the GSC is shorter than L_p noise reduction is modest or nil, whereas when the GSC is longer than L_p noise reduction is substantial. This observation can be used as a rule of thumb in predicting the acoustic benefit of a nozzle arrangement

The mean flow trends measured experimentally have been distilled into a simple model for predicting the convective Mach number distributions. This model can be used for further guidance in assessing the noise reduction potential of various jet configurations. Currently one can examine the average value of M_c within a certain distance, say in the first twenty jet diameters. In that sense, the deflected jet achieves the lowest average Mach number. It also achieves the best noise reduction. A lot of additional work remains to be done before arriving at a reasonably complete model of noise reduction. The average convective Mach number is too simplistic a metric. Additional factors include the amplitude (size) distribution of the eddies, the thickness of the GSC, and the non-uniformity of the velocity distribution within the GSC.

Acknowledgments

The support by NASA Glenn Research Center is gratefully acknowledged (Grant NAG-3-2345 monitored by Dr. Khairul B. Zaman).

References

[1] Tam, C.K.W., and Chen, P., "Turbulent Mixing Noise from Supersonic Jets," *AIAA Journal*, Vol. 32, No. 9, 1994, pp. 1774-1780.

[2] Tam, C.K.W., "Jet Noise: Since 1952," *Theoretical and Computational Fluid Dynamics,* Vol. 10, 1998, pp. 393-405.

[3] Crighton, D.G. and Huerre, P., "Shear-Layer Pressure Fluctuations and Superdirective Acoustic Sources," *Journal of Fluid Mechanics*, Vol. 220, 1990, pp. 355-368.

[4] Avital, E.J., Sandham, N.D, and Luo, K.H., "Mach Wave Radiation in Mixing Layers. Part I: Analysis of the Sound Field," *Theoretical and Computational Fluid Dynamics*, Vol. 12, 1998, pp. 73-90.

[5] Papamoschou, D. and Debiasi, M., "Directional Suppression of Noise from a High-Speed Jet," *AIAA Journal*, Vol. 39, No. 3, 2001, pp. 380-387.

[6] Murakami, E. and Papamoschou, D. "Mean Flow Development of Dual-Stream Compressible Jets," *AIAA Journal*, Vol. 40, No. 6, 2002, pp. 1131-1138.

[7] Dahl, M.D. and Morris, P.J., "Noise from Supersonic Coaxial Jets, Part 1: Mean Flow Predictions," *Journal of Sound and Vibration*, Vol. 200, No. 5, 1997, pp.643-663.

[8] Murakami, E. and Papamoschou, D., "Eddy Convection in Supersonic Coaxial Jets," *AIAA Journal*, Vol. 38, No.4, 2000, pp. 628-635.

[9] Savitzky, A. and Golay, M.J.E. "Smoothing and Differentiation of Data by Simplified Least Squares Procesures," *Analytical Chemistry*, Vol. 36, No. 8, 1964, pp. 1627-.

[10] Papamoschou, D., "A New Method for Jet Noise Reduction in Turbofan Engines," AIAA-2003-1059.

[11] Papamoschou, D., and Roshko, A., "The Turbulent Compressible Shear Layer: An Experimental Study," *Journal of Fluid Mechanics*, Vol. 197, 1988, pp. 453-477.

[12] Hileman, J. and Samimy, M. "Turbulence Structures and the Acoustic Far Field of a Mach 1.3 Jet," *AIAA Journal*, Vol.39, No.9, 2001, pp.1716-27.

[13] Narayanan, S., Barber, T.J., and Polak, D.R., "High Subsonic Jet Experiments: Turbulence and Noise Generation Studies," *AIAA Journal*, Vol. 40, No. 3, 2002, pp. 430-437.

Table 1: Nozzle Configurations

Nozzle	D_s/D_p	A_s/A_p	Configuration
A18	1.78	1.40	Arcuate
C14	1.40	0.90	Coaxial
C16	1.58	1.40	Coaxial
C17	1.70	1.80	Coaxial
C20	2.00	2.90	Coaxial
E14	1.40	0.90	Eccentric
E16	1.58	1.40	Eccentric
E17	1.70	1.80	Eccentric
V16	1.58	1.40	Vanes

Table 2: Flow Conditions

Case	M_p	U_p (m/s)	M_s	U_s (m/s)	U_s/U_p
Single	1.50	430	0	0	0.00
R30	1.50	430	0.37	130	0.30
R49	1.50	430	0.60	210	0.49
R67	1.50	430	0.90	290	0.67
R71	1.00	310	0.66	220	0.71

Table 3: Combinations tested

Case	$\dot{m}_s/\dot{m}_p$
Single	0.00
A18R71	1.00
C16R71	1.00
E16R71	1.00
V16R71	1.00
C14R30	0.20
C14R49	0.33
C14R67	0.52
C17R30	0.39
C17R49	0.65
C17R67	1.02
C20R30	0.62
C20R49	1.03
C20R67	1.62
E14R30	0.20
E14R49	0.33
E14R67	0.52
E17R30	0.39
E17R49	0.65
E17R67	1.02

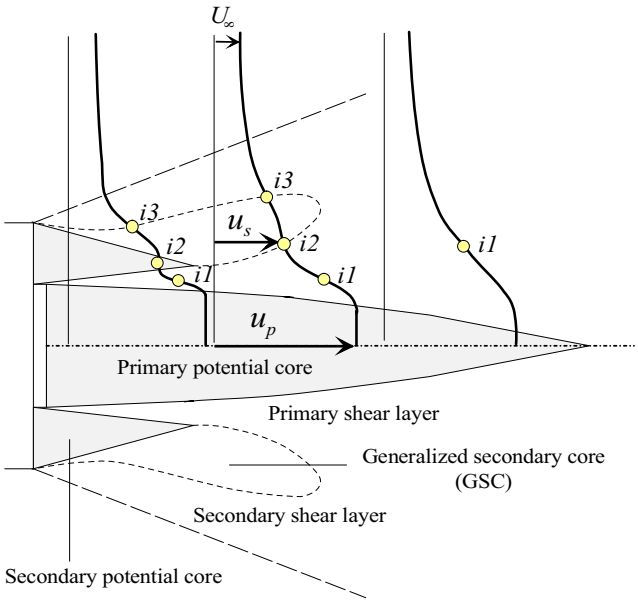

Fig.1 Basic elements of the mean flow in a dual-stream jet.

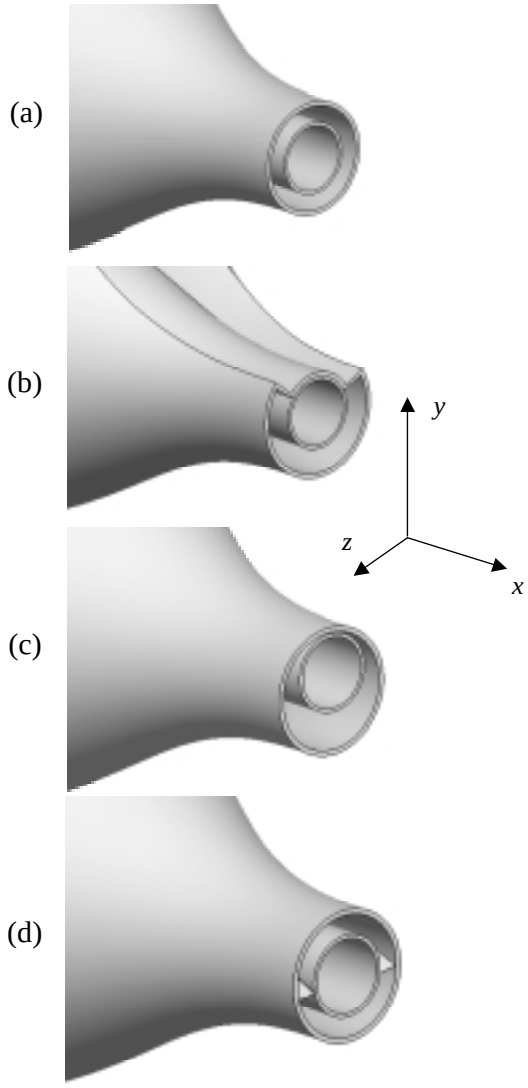

Fig.2 Nozzles used in the mean velocity surveys. (a) coaxial; (b) arcuate; (c) eccentric; (d) coaxial with vanes in the bypass stream. The coordinate system used in the mean flow surveys is shown.

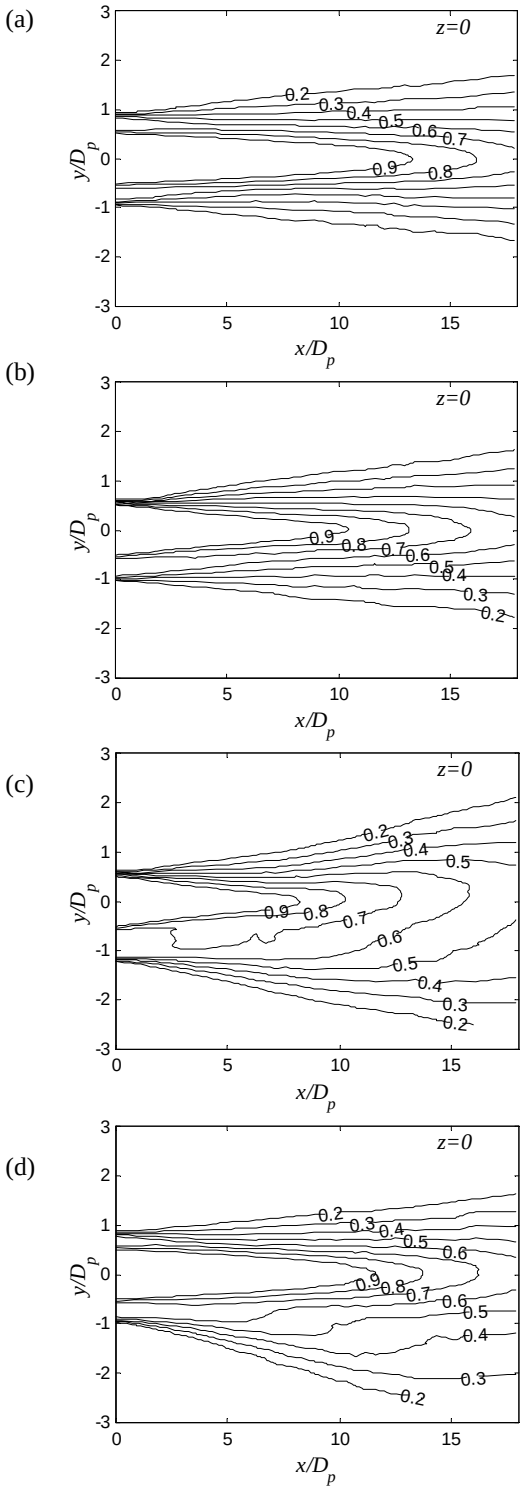

Fig.3 Isocontours of $u(x, y, 0)/U_p$ for the following jets : (a) coaxial (C16R71); (b) arcuate (A18R71); (c) eccentric (E16R71); (d) coaxial with vanes (V16R71).

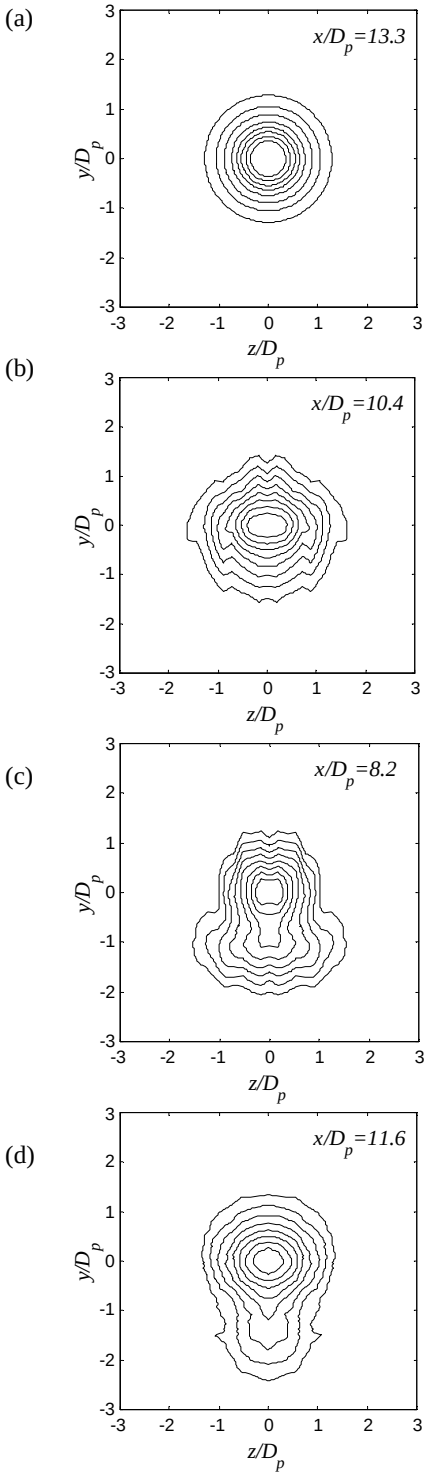

Fig.4 Isocontours of $u(L_p, y, z)/u(L_p, 0, 0)$ for the following jets: (a) coaxial (C16R71); (b) arcuate (A18R71); (c) eccentric (E16R71); (d) coaxial with vanes (V16R71). Levels range from 0.2 to 0.9 in increments of 0.1

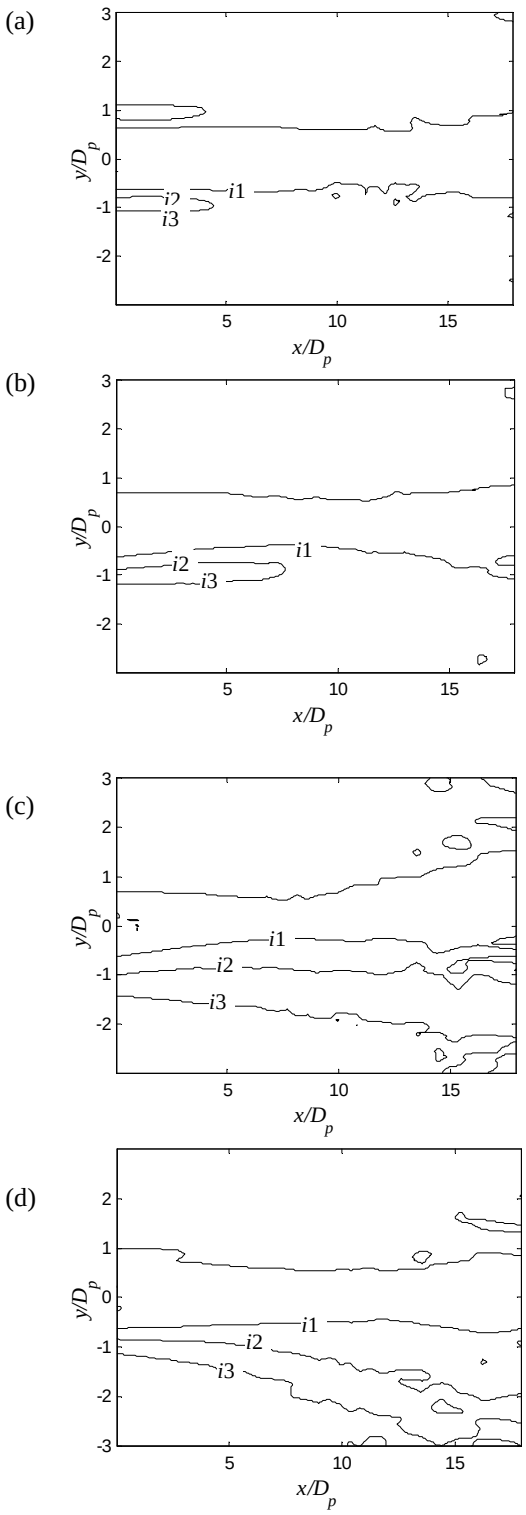

Fig.5 Locus of inflection points for the following jets: (a) coaxial (C16R71); (b) arcuate (A18R71); (c) eccentric (E16R71); (d) coaxial with vanes (V16R71).

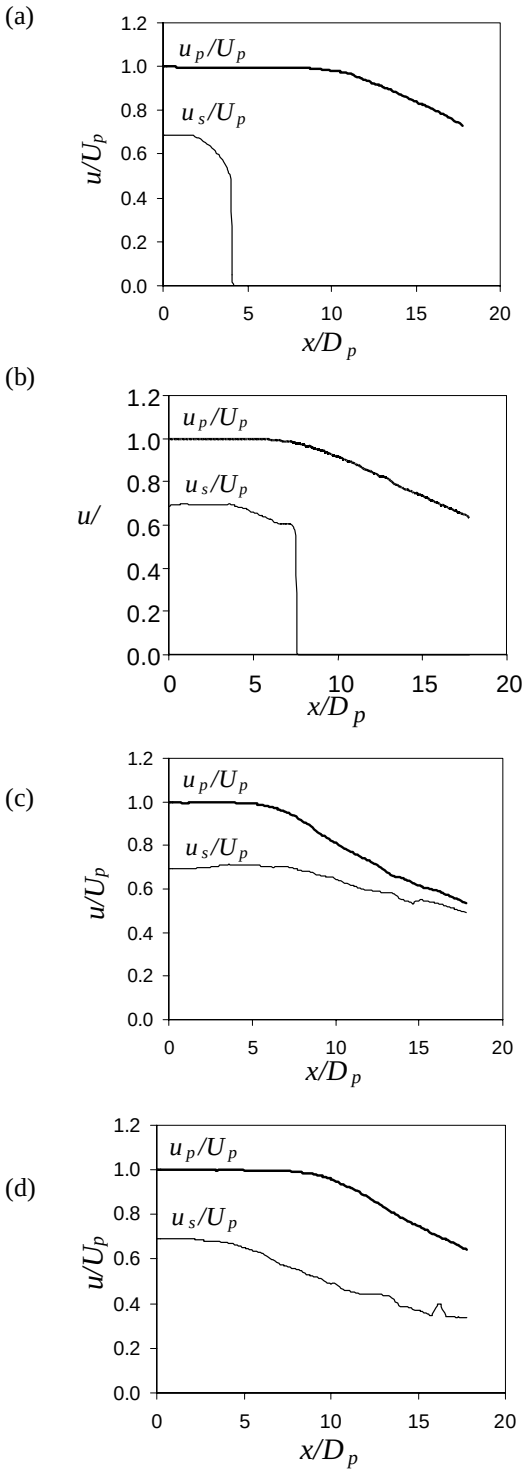

Fig.6 Distribution of velocities defining the primary and secondary shear layers for the jets of Fig. 3. (a) Coaxial jet (C16R71); (b) underside of arcuate jet (A18R71); (c) underside of eccenttric jet (E16R71); and (d) underside of coaxial jet with vanes in bypass stream (V16R71).

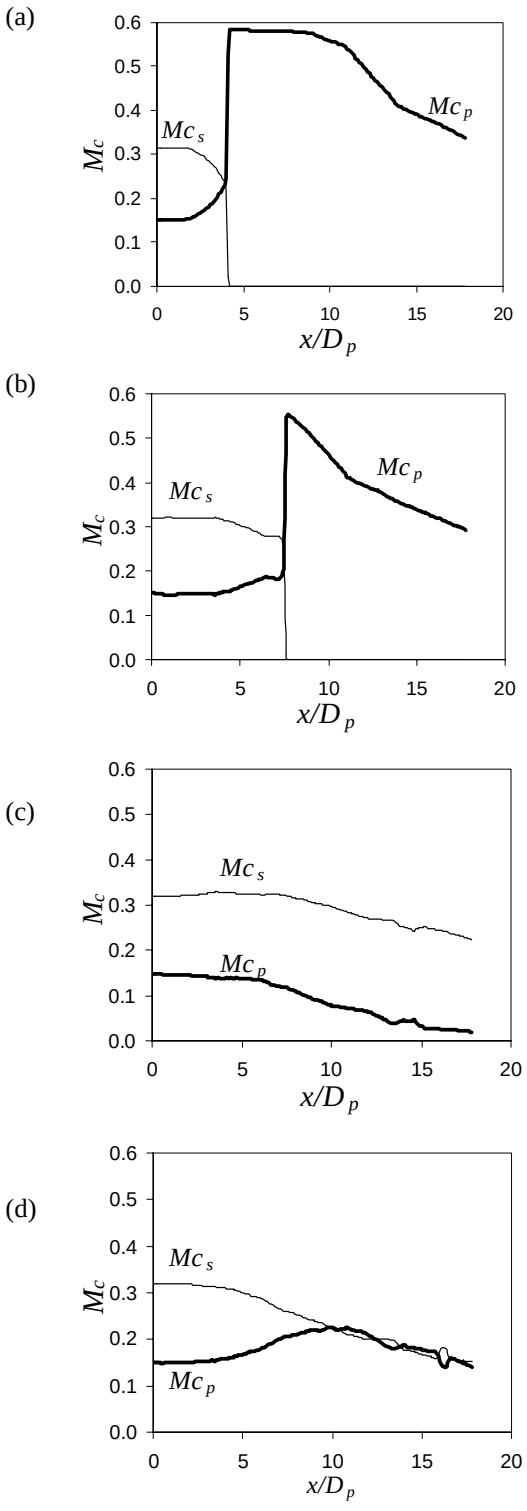

Fig.7 Distribution of convective Mach numbers corresponding to the velocity distributions of Fig. 6. (a) Coaxial jet (C16R71); (b) underside of arcuate jet (A18R71); (c) underside of eccenttric jet (E16R71); and (d) underside of coaxial jet with vanes in bypass stream (V16R71).

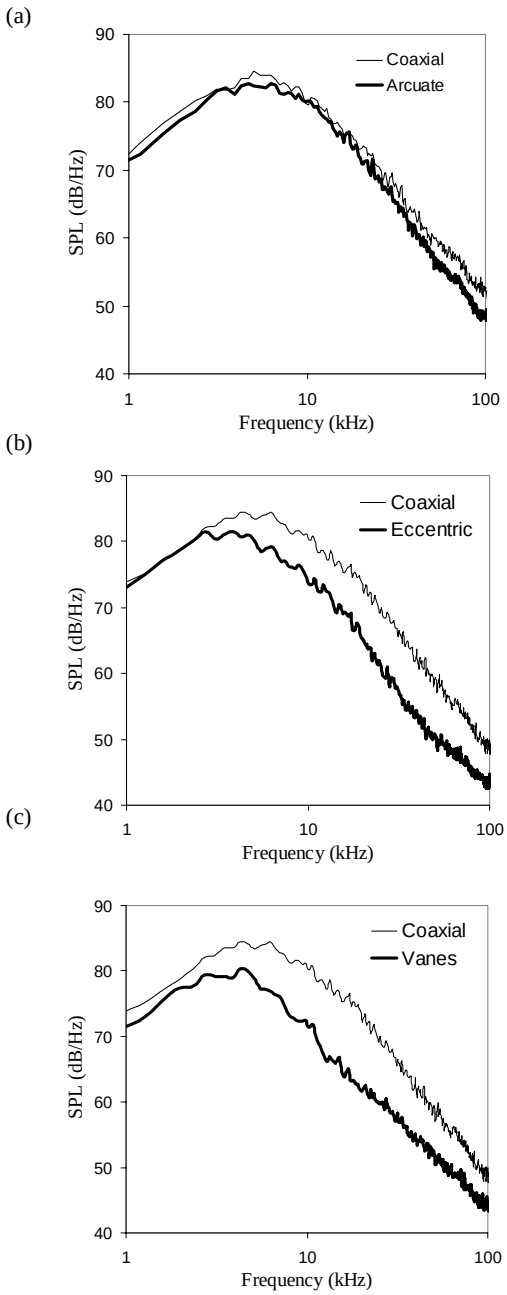

Fig.8 Noise spectra in the direction of peak emission, with comparison to equivalent coaxial case. (a) Arcuate; (b) eccentric; (c) coaxial with vanes in bypass stream.

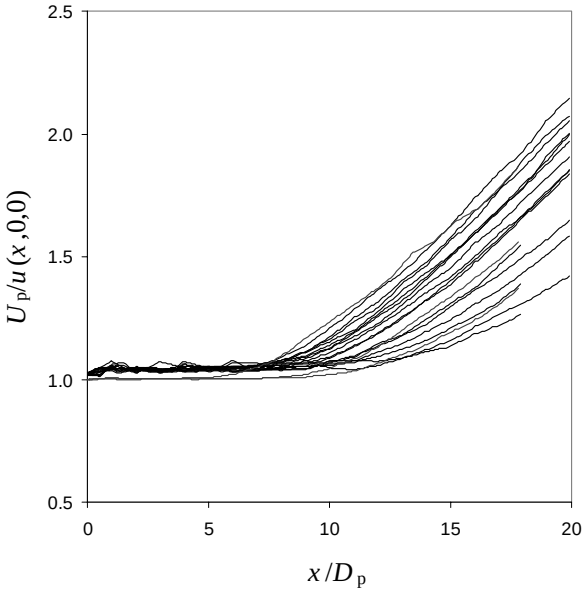

Fig.9 Axial distribution of the reciprocal of the centerline velocity $u_p(x)$ in the absolute frame of reference.

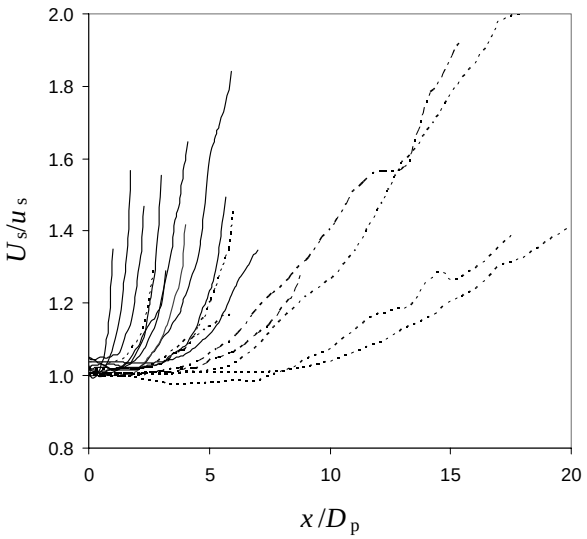

Fig.11 Axial distribution of the reciprocal of the velocity along $i2$, $u_s(x)$, in the absolute frame of reference. Solid lines: coaxial; dotted lines: eccentric; dash-dotted line: vanes.

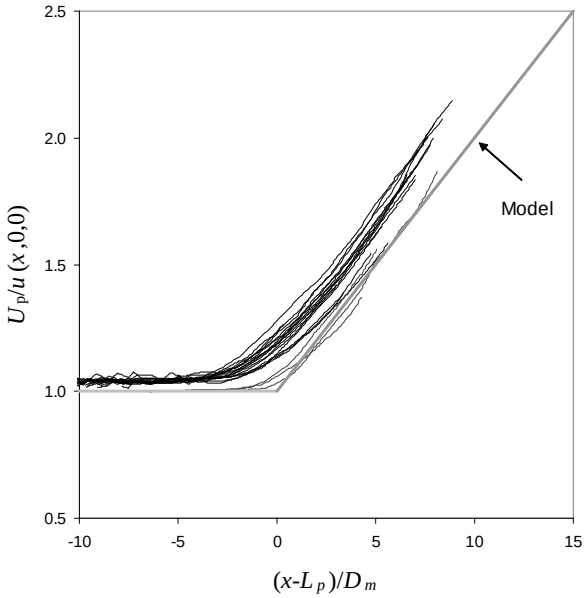

Fig.10 Axial distribution of the reciprocal of the centerline velocity $u_p(x)$ in the proper frame of reference.

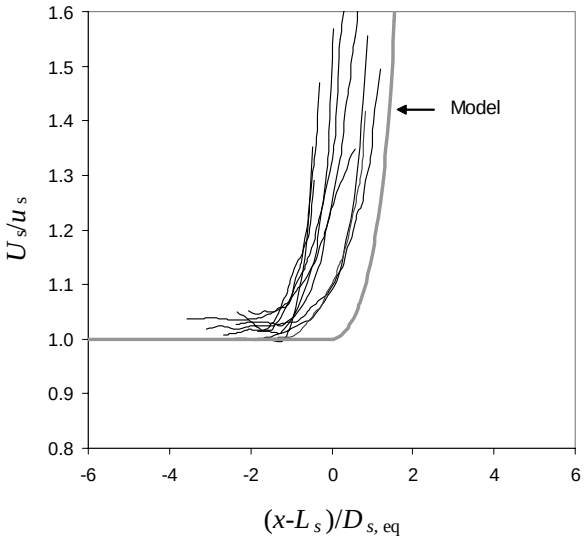

Fig.12 Axial distribution of the reciprocal of the velocity along $i2$, $u_s(x)$, in the proper frame of reference. Coaxial cases only.

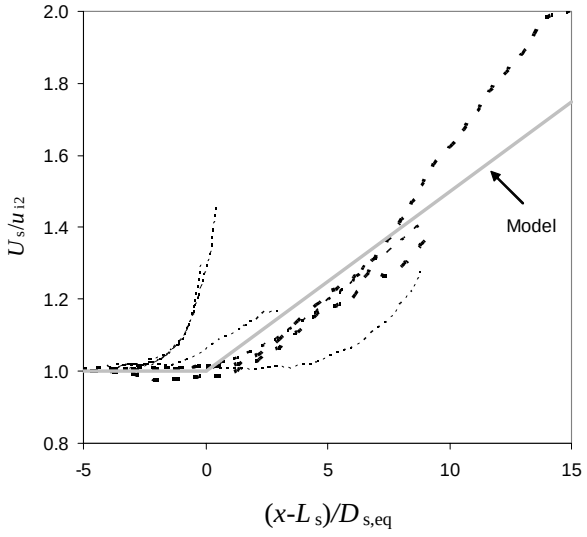

Fig.13 Axial distribution of the reciprocal of the velocity along $i2$, $u_s(x)$, in the proper frame of reference. Eccentric cases only. Heavy lines indicate velocity ratios around 0.7 (R67 and R71).

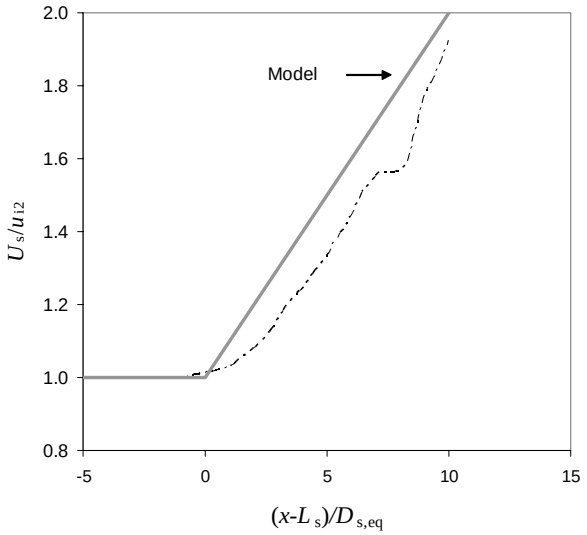

Fig.14 Axial distribution of the reciprocal of the velocity along $i2$, $u_s(x)$, in the proper frame of reference. Coaxial jet with vanes in bypass stream (V16R71).

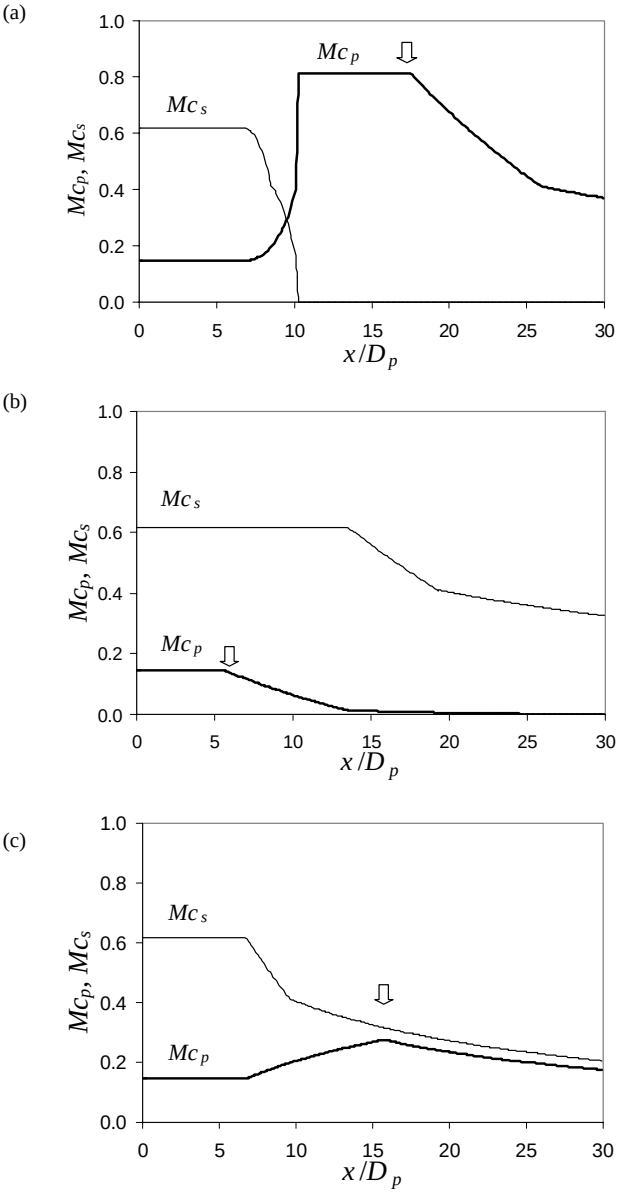

Fig.15 Prediction of convective Mach number distributions for jet from modern turbofan engine at static conditions. (a) Coaxial; (b) eccentric; (c) coaxial with vanes in bypass stream. Arrow indicates end of primary potential core.

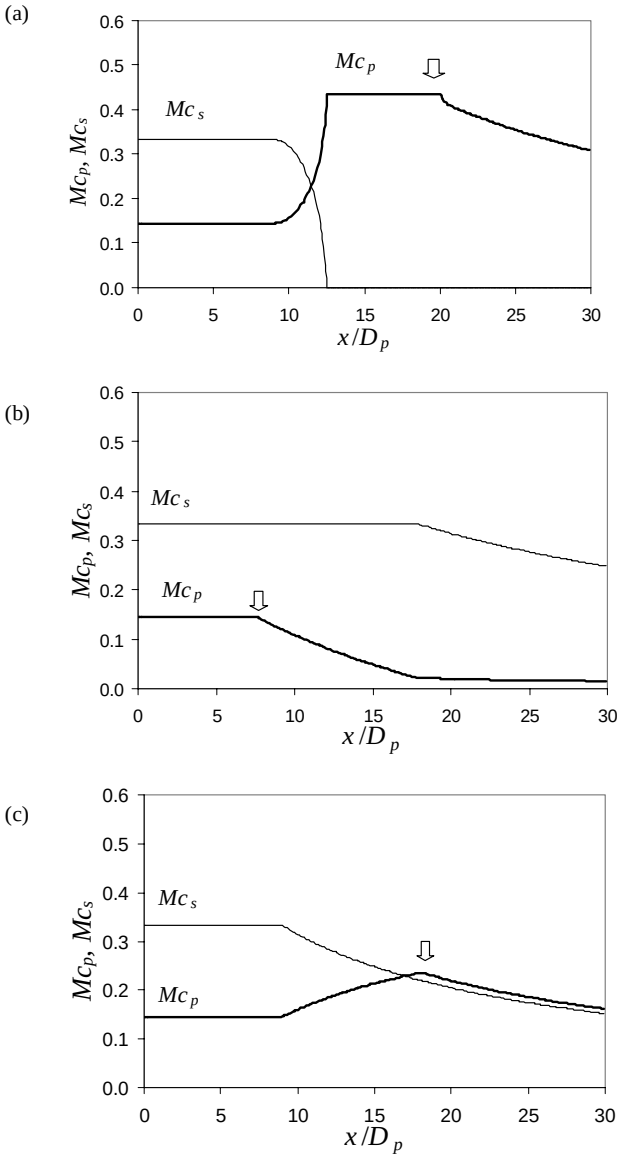

Fig.16 Prediction of convective Mach number distributions for jet from modern turbofan engine at $M_\infty = 0.3$. (a) Coaxial; (b) eccentric; (c) coaxial with vanes in bypass stream. Arrow indicates end of primary potential core.